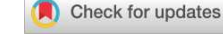
RESEARCH ARTICLE





Heat transfer during droplet impact on a cold superhydrophobic surface via interfacial thermal mapping

Vijay Kumar¹ Qianxi Fu¹ Harrison Szeto² Yangying Zhu¹

Correspondence

Yangying Zhu, Department of Mechanical Engineering, University of California Santa Barbara, Santa Barbara, CA 93106, USA. Email: yangying@ucsb.edu

Funding information

National Science Foundation, Grant/Award Number: 2047727: Office of Naval Research. Grant/Award Number: N00014-24-1-2086

Abstract

Undesired heat transfer during droplet impact on cold surfaces can lead to ice formation and damage to renewable infrastructure, among others. To address this, superhydrophobic surfaces aim to minimize the droplet surface interaction thereby, holding promise to greatly limit heat transfer. However, the droplet impact on such surfaces spans only a few milliseconds making it difficult to quantify the heat exchange at the droplet-solid interface. Here, we employ high-speed infrared thermography and a three-dimensional transient heat conduction COMSOL model to map the dynamic heat flux distribution during droplet impact on a cold superhydrophobic surface. The comprehensive droplet impact experiments for varying surface temperature, droplet size, and impacting height reveal that the heat transfer effectiveness (Q') scales with the dimensionless maximum spreading radius as $Q' \sim (R_{\text{max}}/R_i)^{1.6}$, deviating from previous semi-infinite scaling. Interestingly, despite shorter contact times, droplets impacting from higher heights demonstrate increased heat transfer effectiveness due to expanded contact area. The results suggest that reducing droplet spreading time, as opposed to contact time alone, can be a more effective strategy for minimizing heat transfer. The results presented here highlight the importance of both contact area and contact time on the heat exchange between a droplet and a cold superhydrophobic surface.

INTRODUCTION

Thermal energy transfer between a droplet and a surface can lead to many undesired situations such as ice formation on airplane wings, power transmission lines, renewable infrastructure, and heat loss from the body of animals during rain. 1,2 One way to limit this undesired heat transfer is to make the surface superhydrophobic (SHP).^{2,3} Such surfaces exhibit a contact angle >150° and a very low contact angle hysteresis due to entrapped air within the surface structures.^{4,5} As a result, when a droplet impacts a SHP surface, the droplet quickly bounces back. 5,6 Such a short contact time and contact area have

the promise to limit the heat exchange between the droplet and the surface.³ While the residence or contact time of the droplet on such surfaces is on the order of a few milliseconds, there is still a finite amount of heat transfer. The heat transferred can become significant for a sequence of droplets such as during freezing rain or spray.² Therefore, understanding the heat transfer between a single impacting droplet and the SHP surface is critical to further design surfaces to tune thermal energy transfer.

In general, it is believed that reduced contact area and contact time lead to limited heat transfer. For the purpose of possibly reducing the heat transfer, a variety of hydrophobic and structured surfaces have

This is an open access article under the terms of the Creative Commons Attribution License, which permits use, distribution and reproduction in any medium, provided the original work is properly cited.

© 2024 The Author(s). Droplet published by Jilin University and John Wiley & Sons Australia, Ltd.

¹Department of Mechanical Engineering, University of California Santa Barbara, Santa Barbara, California, USA

²Department of Chemistry and Biochemistry, University of California Santa Barbara, Santa Barbara, California, USA

been developed^{3,7-16} focusing on reducing the contact time and contact area. Shiri and Bird² reported a reduction in contact time using surface structures that redistribute the liquid mass asymmetrically and hence alter the drop hydrodynamics. Tao et al.¹⁰ fabricated inclined Janus structures to reduce the contact time during droplet impact. In other studies, asymmetric spreading of a droplet upon impact on inclined, moving, and vibrating SHP surfaces was shown to reduce the contact time.^{15,17-20} Mishchenko et al.³ reported that carefully designed nanostructured SHP surfaces can prevent ice formation at low temperatures by reducing both contact area and contact time. While these studies highlight the importance of micro-/nanostructures to tune the hydrodynamics of a droplet during surface contact, the resulting heat exchange needs to be further quantified.

A few recent studies^{2,21–25} have specifically investigated the heat transfer during a drop impact on SHP surfaces. The heat transfer analysis presented therein utilized infrared (IR) imaging, however, often relied on measuring droplet surface temperature,^{25,26} assumed uniform temperature into the substrate,²² or the surface temperature after the droplet has left the surface.^{2,21} Such indirect interpretation may not provide accurate quantification of the solid-liquid interface heat transfer. Further, several previous studies^{2,27,28} utilized a semi-infinite model that relies on the area-averaged temperature to predict the heat transfer. While insightful, a semi-infinite model may not provide accurate spatial information. An accurate quantification would require a spatiotemporally resolved, noninvasive temperature measurement technique, along with accurate transient heat transfer estimation during the short droplet–substrate contact duration.

Recently, some studies^{29–33} have reported a detailed methodology to interpret the solid-liquid interface temperature using IR imaging. For instance, Bucci et al.²⁹ used an IR-transparent substrate to measure the temperature of the IR-opaque solid-liquid interface. The study developed a coupled conduction-radiation model to infer the spatially resolved surface heat flux during phase change heat transfer. Li and Weisensee³⁰ used IR imaging to measure the solid-liquid interface temperature during drop impact on a hydrophobic surface. The study used a finite volume method to estimate the surface heat flux and highlighted the localized high heat flux at the contact line. While the contact line heat flux plays an important role on a heated hydrophobic surface, it may not have a similar effect on the SHP surfaces. Gholijani et al.³¹ measured the interface temperature and derived the associated heat flux to study the role of liquid surface tension, substrate temperature, surface roughness, and droplet size on a heated hydrophilic surface. While the methodology presented in these studies can be generalized, the heat exchange between a drop impacting a cold SHP surface may be fundamentally different due to the lack of phase change near the three-phase contact line.

In this paper, we employ high-speed infrared thermography synchronized with high-speed fluid morphology to quantify the transient solid-liquid interface heat transfer during a droplet impact on a cold SHP surface. To obtain the transient heat transfer during the entire droplet impact process, we specifically focus on the experiments wherein the droplet does not freeze on the surface before bouncing. We use an IR-transparent substrate which allows the IR camera

to accurately measure the temperature at the solid-liquid interface. Unlike previous area-averaged approaches, we import the spatially and temporally resolved two-dimensional (2D) temperature maps to a three-dimensional (3D) transient heat conduction model in COMSOL to accurately simulate the 3D temperature distribution and spatially resolved surface heat flux. We focus on interpreting the detailed role of contact area and contact time on transient heat transfer. For this, we perform experiments at various droplet impacting heights, substrate temperature ($\Delta T = 10-20$ K), and droplet size ($R_i \approx 0.5-1$ mm). Our results show that the heat transfer effectiveness scales with the dimensionless maximum spreading radius R_{max}/R_i as $Q' \sim (R_{\text{max}}/R_i)^{1.6}$, different than previous semi-infinite scaling of $(R_{\text{max}}/R_i)^2$. Further, the presence of an air layer on SHP surfaces manifests as an additional thermal resistance, highlighting the importance of the actual contact area. Interestingly, we also show that for a given droplet size, droplets with a higher impacting height provide more effective heat transfer despite having shorter contact time. This can be attributed to a dominant role played by the increase in contact area during spreading, with increasing height. Overall, we show that just a reduction in the overall contact time may not be sufficient to reduce the heat transfer. Instead, reducing the droplet spreading time can be more beneficial. The results reported in this study highlight the important role of both contact area and contact time on the heat exchange between a droplet and a cold SHP surface.

RESULTS AND DISCUSSION

First, we demonstrate temporally and spatially resolved high-speed optical and infrared imaging for a droplet impacting a cold SHP surface (Figure 1). A simplified schematic of the experimental setup is shown in Figure 1a, while the details of the experimental process are provided in Supporting Information S1. Briefly, a sealed chamber is purged with room temperature (RT) nitrogen to maintain a constant environmental temperature and low humidity (Figure 1a); an IR-transparent sapphire substrate (transmission details in Supporting Information S9) coated with a thin layer of IR-opaque black paint and hydrophobic microspheres (referred to as an SHP coating; Figure 1b) is cooled to a set temperature using cold nitrogen gas beneath. The SHP surface shows a contact angle of $\approx 160^{\circ}$ with a very low contact angle hysteresis of $< 5^{\circ}$. Details of the fabrication steps and wettability characterization of the SHP surface are provided in Supporting Information S1. The temperature of the black paint is probed using a high-speed IR camera (Telops, M3K; see the blue arrows in Figure 1a). Then, a droplet is dispensed on the surface from a set height. The droplet impacting dynamics are recorded using a high-speed camera (Phantom, Veo 640) from the side, which provides the initial droplet diameter, velocity at impact (Figure 1c,i), velocity during spreading (Figure 1c,ii), the maximum spreading diameter D_{max} (Figure 1c,iii), and the droplet bounce-off time also known as contact time t_c (Figure 1c,iv). In Figure 1c, the surface is maintained at 278 K to represent a low-temperature scenario, and the RT droplet ($T_1 = 298 \text{ K}$) with a diameter of $\sim 2 \text{ mm}$ is dispensed from a height of 9 cm. Simultaneously, the black paint temperature

FIGURE 1 Experimental setup and the resulting optical and thermal characterization. (a) Schematic of the experimental setup. Room temperature (RT) nitrogen maintains a constant temperature in the test chamber, while a high-speed (HS) infrared (IR) camera images the temperature of the droplet–surface interface. (b) Scanning electron microscope (SEM) image of the superhydrophobic surface. (c) High-speed optical images of a droplet impacting and bouncing on the superhydrophobic (SHP) surface. In this case, the initial temperatures of the surface (T_s) and the droplet (T_t) are 278 and 298 K, respectively. The initial droplet diameter is ~ 2 mm, impacting height (t) is 9 cm and contact time is 10 ms. (d) Simultaneous temperature map at the solid–liquid interface, acquired from the bottom view, corresponding to the plane shown with a blue dash line in (t). The corresponding: (e) temperature profile into (cross-section) the substrate, at the white dashed line in (t), (t) spatially resolved surface heat flux, and (t) heat flux within the substrate are estimated using COMSOL simulation.

captured by the IR camera is assumed to be the drop-substrate interface temperature (Figure 1d) due to its minimal thickness. The emissivity (ε) of the black paint was calibrated to be 0.95, using a J-type thermocouple (Supporting Information S2). The blue dashed line in Figure 1c,i depicts the IR imaging plane for the corresponding temperature maps. Based on the spatially resolved solid-liquid interface temperature measured during impact, the 3D temperature in the substrate (Figure 1e, cross-sectional temperature at white dashed line in Figure 1d) and heat flux on the surface and within the substrate (Figure 1f,g) are extracted using COMSOL multiphysics as explained next.

In order to obtain the heat flux at the droplet–substrate interface using the measured dynamic temperature distribution, we employ the heat transfer module in COMSOL to solve the 3D temperature and heat flux profiles at each time step. The methodology is similar to the finite element approach by Li and Weisensee³⁰ and is briefly described here. First, we generate a 3D block of sapphire with dimensions the same as the IR camera window size in experiments (Figure 2a). The spatiotemporally varying surface temperature captured by the IR camera is then imported as the top surface boundary condition of the sapphire ($T_{IR}(x,y,z_o,t)$) as shown in Figure 2a. This allows the top surface to always represent the solid–liquid interface temperature during the impact, wherein the heat conducts into the sapphire substrate. Due

to the small timescale of the impacting process, the sides are modeled as adiabatic. Given that the cold nitrogen flow is stopped before the droplet impact, the bottom surface can be assumed as a natural convection boundary condition with a heat transfer coefficient (h_b) of 10 W/m² K. Note the heated zone does not propagate to the sides or the bottom of the substrate for the duration of droplet impact, as shown in Figure 2b. Therefore, the 3D heat transfer analysis is not particularly sensitive to the side and bottom boundary conditions in COMSOL. The heat Equation (1) is solved, which produces a time-dependent 3D temperature profile T(x, y, z, t). In Equation (1), k_s , ρ_s , and c_s are the thermal conductivity, density, and specific heat capacity of the substrate, respectively.

$$\nabla \cdot k_{s} \nabla T(x, y, z, t) = \rho_{s} c_{s} \frac{\partial T(x, y, z, t)}{\partial t}.$$
 (1)

Once a converged 3D temperature profile is obtained, the surface heat flux at each time step is then calculated using Fourier's law (Equation 2):

$$q_s''(x, y, z_o, t) = -k_s \frac{\partial T_{IR}(x, y, z_o, t)}{\partial z_o},$$
 (2)

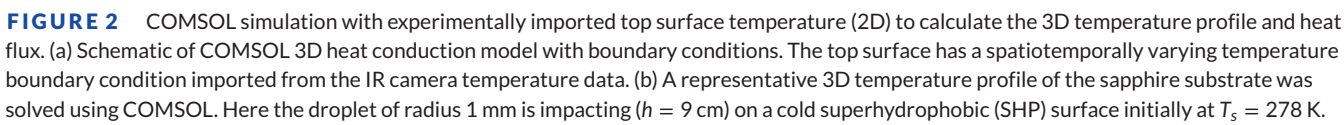
where, $T_{IR}(x,y,z_o,t)$ is the instantaneous surface temperature from the IR camera, and $\frac{\partial T_{IR}(x,yz_o,t)}{\partial z_o}$ is the temperature gradient in the z direction

 $T_{IR}(x, y, z_o, t)$

 $S_{apphire}$

 $h_{\rm b}, T_{\rm b}$

(a)



at the surface (z_o) solved by COMSOL. A representative 3D temperature contour profile is shown in Figure 2b. The details of the COMSOL model and thermophysical properties are provided in Supporting Information S3 and Table S1. Based on this methodology, the estimated 3D temperature and heat flux profiles for a RT water droplet impacting on an SHP surface ($T_s = 278 \text{ K}$, h = 9 cm, $R_i = 1 \text{ mm}$) are shown in Figure 1e-g, respectively. The short interaction of a droplet with our SHP surface results in temperature rise localized to the surface and high spatial temperature gradients of ~ 35 K/cm (evaluated, at the surface, from Figure 2b) in the z-direction. While the droplet is in contact with the surface for 10 ms, the maximum local heat flux occurs during droplet spreading (see Figure 1f,ii) and the heat flux remains small during retraction. This suggests a thinner thermal boundary layer thickness during spreading.

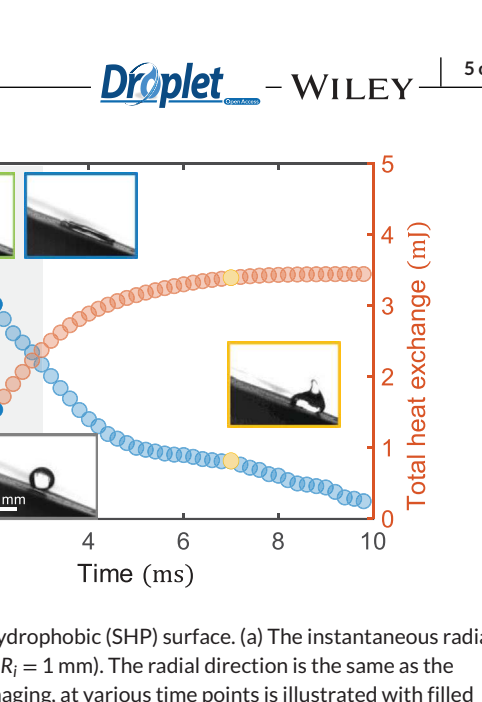
To further illustrate, the radial heat flux $q_s''(r, t)$ and surface-averaged heat flux \bar{q}_s'' during the droplet impact ($T_l = 298 \text{ K}, T_s = 278 \text{ K}, h = 9 \text{ cm}$, $R_i = 1$ mm) are shown in Figure 3. Note that the radial heat flux is extracted from the top surface (z_o) and along the white dashed line in Figure 1d. Figure 3a shows that the spreading stage has higher local heat flux (t = 1 ms green markers and t = 2 ms blue markers) as compared to the retraction stage (t = 4 ms purple markers and t = 7 ms yellow markers). The highest heat flux exceeded 20 W/cm² during the initial contact ($t \approx 1$ ms). The instantaneous droplet spreading radius r(t) corresponding to each time stamp is illustrated by the bar chart in Figure 3a. Unlike a droplet impacting a heated surface where the contact line can have an order-of-magnitude higher heat flux due to rapid evaporation, 15 the contact line heat transfer does not play a significant role during droplet impact on cold SHP surfaces. Rather, the highest heat flux occurred near the center of the droplet during the initial impact ($t \approx 1$ ms), presumably due to a minimal thermal boundary layer thickness (schematic in Supporting Information S8) near the stagnation point and an increasing thickness of the thermal boundary layer towards the edge of the droplet (schematic shown in Supporting Information S8). At t = 2 and 4 ms, the heat flux is relatively uniform along the radial direction with no visible high heat transfer at the droplet contact line during spreading or receding. As shown in Figure 3b, the averaged heat flux ($\bar{q}_s''(t)$, blue markers in Figure 3b)

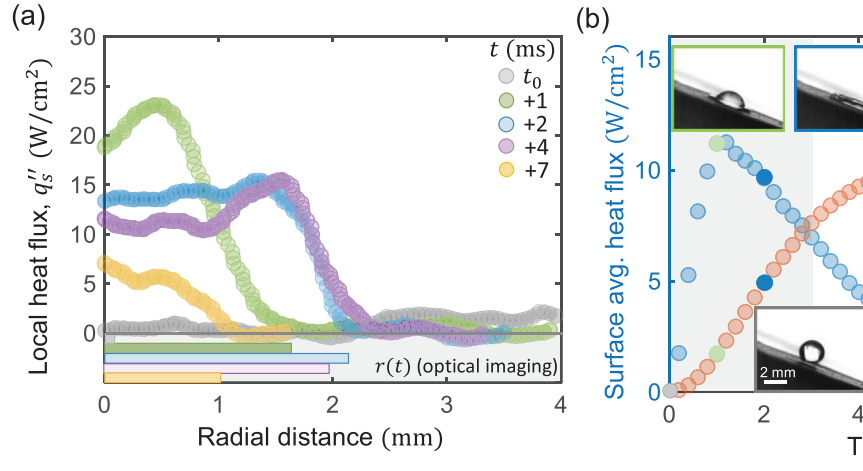
over the instantaneous droplet contact area, quickly reaches maxima within 1 ms of droplet contact and thereafter decreases monotonically during the rest of the spreading stage (the gray-shaded region in Figure 3b) and retraction stage (the unshaded region in Figure 3b). The temporally asymmetric heat flux $\bar{q}_s''(t)$ distribution suggests that, despite a short timescale (~3 ms), the spreading stage may contribute more to the total heat exchange. The total heat exchange Q(t) over time (orange markers in Figure 3b), defined by integrating the surface heat flux over the contact area (A) and time using Equation (3), suggests that the spreading stage contributes ~65% to the total heat transfer (end of the gray-shaded region in Figure 3b representing the maximum spreading).

$$Q(t) = \int \int_{t=0}^{t} q_s'' dA dt.$$
 (3)

Further, during the retraction stage, the heat flux quickly becomes negligible even before the droplet bounces off the surface (see the yellow marker and the corresponding optical image in Figure 3b). The findings discussed in this section are applicable to all the experimental conditions conducted in this study. Such highly transient heat transfer has important consequences, explained later in the text. To illustrate the dynamic heat transfer process, a synchronized high-speed optical, thermal, and 3D heat flux video is provided in Supporting Information

Next, we highlight the contribution of the contact area on the total heat exchange between the drop and the cold SHP substrate. The total heat exchange (Q) calculated using Equation (3) for different droplet sizes, substrate temperature, and impact height is shown in Figure 4a. Clearly, the larger droplets ($R_i = 1$ mm) have higher total heat exchange compared to droplets with $R_i = 0.5$ mm. This happens because, for a given impact height, the larger radius droplet spreads more upon impact onto the surface and hence has a larger contact area for heat transfer. Note that the heat flux remains similar among different drop sizes (for similar surface temperatures). For a given droplet size, Q increases with impacting height and the initial temperature difference between the drop and the substrate ($\Delta T = T_l - T_s$). For larger impact height, the droplet has a higher kinetic energy and spreads





Detailed thermal energy exchange during a droplet impact on a cold superhydrophobic (SHP) surface. (a) The instantaneous radial heat flux during the drop impact on the cold SHP surface ($T_i = 298 \text{ K}$, $T_s = 278 \text{ K}$, h = 9 cm, $R_i = 1 \text{ mm}$). The radial direction is the same as the white-dashed line in Figure 1d. The contact radius r(t), captured using high-speed optical imaging, at various time points is illustrated with filled horizontal bars at the bottom of the figure. (b) Surface average heat flux (based on the instantaneous droplet contact area) and total heat transfer during various stages of droplet impact. Gray (at impact), green (spreading stage), blue (spreading stage), and yellow (retraction stage) filled markers correspond to optical images during various stages of droplet impact. Note that the color and time instant for these markers is the same as in (a).

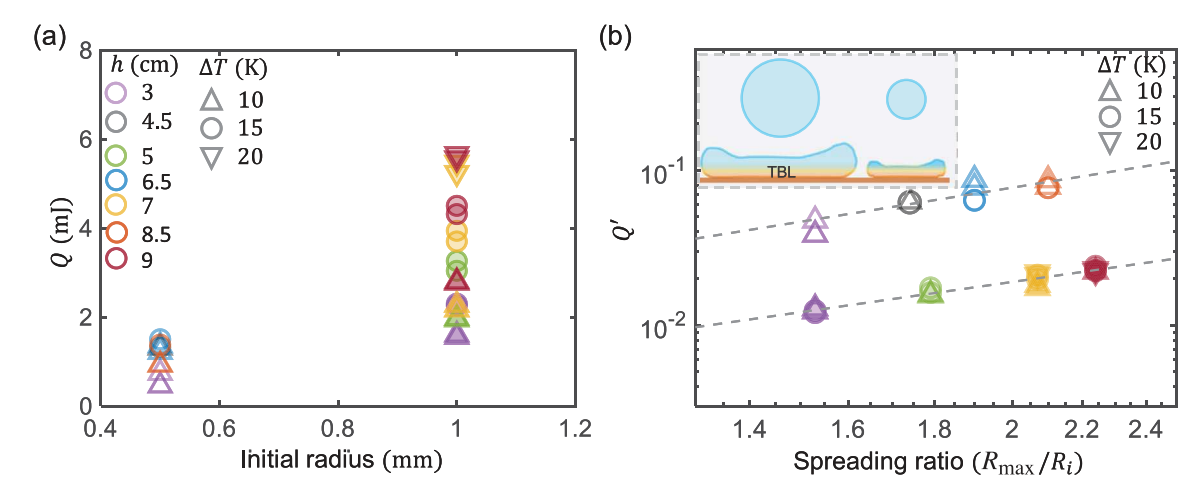


FIGURE 4 The dependence of total heat exchange on contact area. (a) Total heat exchange (Q) during drop impact on the superhydrophobic (SHP) surface for different drop sizes, substrate cooling (ΔT), and impact height. Note that for a single drop size, the data contain various impact heights (h) and the initial temperature difference (ΔT) between the substrate and the drop, hence a spread in the data. The color of the data markers represents h (regardless of the shape), and the shape of the data markers represents ΔT (regardless of the color). (b) Normalized heat exchange (Q') dependency on the spreading ratio (R_{max}/R_i). R_{max} is the maximum spreading radius, and R_i is the initial drop radius. Filled symbols represent a 1 mm radius drop, and open symbols represent a 0.5 mm radius drop. The dashed lines represent the power law relation of $Q' \sim \left(R_{\rm max}/R_i\right)^{1.6}.$

farther on the surface thereby, providing a larger contact area. A better comparison of Q among various experimental conditions can be realized by nondimensionalizing Q with the maximum possible thermal energy transfer $(mc_p(T_l - T_s))$ or $mc_p\Delta T$, adapted from previous literature:

$$Q' = \frac{Q}{mc_p\Delta T},$$
 (4)

where m is the mass of the droplet $(\frac{4}{3}\pi R_i^3 \rho_I)$, c_p is the specific heat capacity of water, and ρ_l is water density. The normalized total heat

transfer (Q') is also referred to as heat transfer effectiveness, that is, the amount of thermal energy exchanged out of total available thermal energy. To understand the impact of droplet spreading on heat transfer we next plot Q' with the spreading ratio (R_{max}/R_i) , as shown in Figure 4b. While the total heat exchange (Q) is higher for larger droplets (filled symbols in Figure 4a), the normalized Q' (effectiveness) is higher for smaller droplets (open symbols in Figure 4b). The drops with 0.5 mm radius exchange approximately three to four times higher thermal energy out of the possible energy transfer $(mc_p\Delta T)$, as compared to the 1-mm radius droplets. Here, the initial volume ($V_i = \frac{4}{3}\pi R_i^3$)

Effect of the insulating air layer between impacting drop and superhydrophobic (SHP) surface. Effective thermal resistance comparison during droplet impact on the (a) SHP surface and (b) rough hydrophobic (RHP) surface. The presence of an almost continuous air layer trapped in between the drop and the surface results in poor effective thermal conductivity (k_{eff}) of the SHP surface. (c) The effective thermal conductivity ($k_{\rm eff}$) as a function of the spreading ratio. The data points in the gray-shaded region represent $k_{\rm eff_{SHP}}$ for various spreading ratios. Data points in the yellow-shaded region represent $k_{\rm eff_{RHP}}$ for various spreading ratios. Data points in the blue-shaded region represent $k_{\rm eff_{HP}}$ for various spreading ratios. Different marker colors signify impact height (h) same as in Figure 4a. (d) Scanning electron microscope (SEM) images for SHP, RHP, and smooth hydrophobic (HP) surfaces. The scale bar in all SEMs is the same at 2 µm.

to spreading surface area ($A_{\rm max}=\pi R_{\rm max}^2$) ratio for smaller droplets is higher. Therefore, for a given spreading ratio the droplets with lower initial volume have more liquid mass (relative to the initial droplet mass) within the thermal boundary layer (TBL). For instance, for a $R_{\text{max}}/R_i = 2$ the V_i/A_{max} ratio is 3 for larger droplet ($R_i = 1$ mm) and 6 for smaller droplet ($R_i = 0.5$ mm), which can also be verified from the high-speed optical snapshots (Supporting Information: Figure S3) of the drop impact process. The inset in Figure 4b illustrates the TBL during the spreading of two different-sized drops and explains the better effectiveness of smaller droplets. Comparing the V_i/A_{max} ratio suggests that 0.5 mm radius droplets are twice as effective as 1 mm radius droplet, close to our experimental observations.

Further, our spatiotemporally resolved heat transfer analysis shows that the heat transfer effectiveness empirically scales as $Q'\sim$ $(R_{\text{max}}/R_i)^{1.6}$. The heat flux relation here is lower than predicted by the semi-infinite model, $Q' \sim (R_{\text{max}}/R_i)^{2.2}$ We attribute this discrepancy to the sub-optimal fitting of the semi-infinite model to the spatiotemporally resolved temperature mapping (Supporting Information: Figure S5b). While the semi-infinite model works well in capturing the temperature decay after the droplet has left the surface (Supporting Information: Figure S5c), it does not capture the complex heat transfer process during droplet impact. The details of semi-infinite model fitting are provided in Supporting Information S6.

Additionally, on SHP surfaces the actual contact area of a droplet can be significantly lower than the apparent contact area (Figure 5a). Such reduction in actual contact area along with the low thermal conductivity trapped air has the potential to greatly alter the thermal resistance ($R_{\text{eff}_{SHP}}$ in Figure 5a) and hence the heat transfer during a droplet impact. To understand the effect of a trapped air layer between an impacting droplet and an SHP surface, we estimate the effective thermal conductivity of an SHP surface based on the heat flux and the

temperature gradient upon initial impact ($t \sim 0$) using Equation (5):

$$k_{\text{eff}} = \frac{q_{s,i}''}{\frac{T_{\text{int,i}} - T_{s,i}}{q}},$$
 (5)

where $k_{\rm eff}$ is the effective thermal conductivity between the black paint layer and the drop (Figure 5a), $q_{si}^{"}$ is the initial heat flux upon contact, $T_{\text{int},i}$ is the initial drop bottom surface temperature as it impacts the SHP surface, $T_{s,i}$ is the initial substrate temperature measured by the IR camera, and d is the thickness of the SHP coating with the trapped air cavities (Figure 5a). While T_{int,i} is unknown, for the purpose of approximating k_{eff} and maintaining consistency in calculations across various experiments, we assume T_{int} to be the same as the initial drop temperature (T_l) due to a negligibly thin thermal boundary layer thickness at $t \sim 0$. We then plot $k_{\rm eff}$ against $R_{\rm max}/R_i$ under various impacting conditions (the gray-shaded region in Figure 5c). We then compare $k_{\rm effSHP}$ with effective thermal conductivity of a droplet impacting a rough hydrophobic (RHP) surface (the yellow-shaded region in Figure 5c). The RHP (SEM in Figure 5d) surface used herein is fabricated with a similar recipe as for the SHP surface without the nanostructures (details in Supporting Information S7). This results in the droplet spreading to its maximum diameter and then only partially retracting, unlike the SHP surface where a drop fully retracts and bounces back. The calculated effective thermal conductivity for both surfaces (RHP and SHP) is shown in Figure 5c.

A comparison between $k_{\rm eff_{SHP}}$ (data points in the gray-shaded region in Figure 5c) and $k_{\rm eff_{RHP}}$ (data points in the yellow-shaded region in Figure 5c) highlights that the trapped air between the impacting droplet and the SHP surface results in a lower effective thermal conductivity and hence a lower heat transfer. It is possible that the RHP surface may still have some air trapped in the roughness cavities (a)

0.4

0.35

0.3

0.2

0.15

0.1 8

9

10

○ 0.25

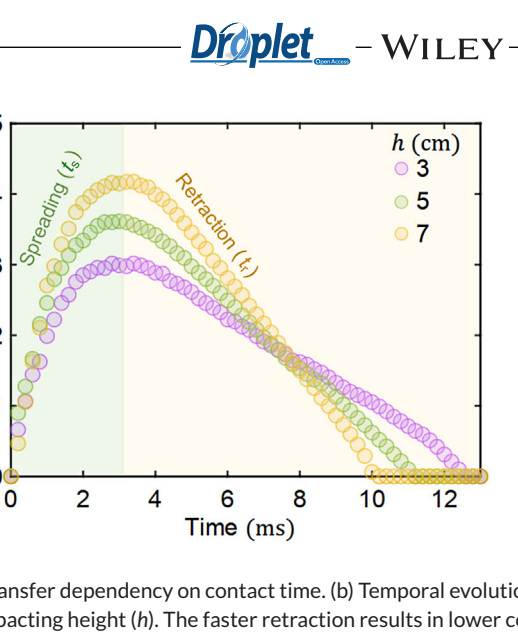


FIGURE 6 Heat transfer dependency on contact time. (a) Normalized heat transfer dependency on contact time. (b) Temporal evolution of the droplet diameter highlighting faster retraction of drops impacting with higher impacting height (h). The faster retraction results in lower contact time for droplets impacting with greater height.

13

(b)

Diameter (mm)

h (cm)

3

5

7

00

11

Contact time (ms)

 ΔT (K)

 $\Delta 10$

015

 ∇ 20

00

12

5

(as shown in the schematic in Figure 5b); therefore, to further substantiate the impact of trapped air, we fabricate a smooth hydrophobic surface (HP) using only polydimethylsiloxane (PDMS) spin coating (SEM in Figure 5d and fabrication details in Supporting Information S7). The HP surface may not trap any air due to lack of roughness cavities and would result in even higher $k_{\rm eff_{\rm HP}}$ (shown in the blue-shaded region in Figure 5c) as compared to $k_{\rm eff_{RHP}}$ (shown in the yellow-shaded region in Figure 5c). The heat flux for HP, RHP, and SHP surface used to calculate the effective thermal conductivity is shown in Figure S4 in Supporting Information. These results highlight that both the apparent maximum spreading (macroscopic) and actual contact area (microscopic) play an important role in determining the total heat transfer between a droplet and the surface. Interestingly, while our experiments show a positive correlation between heat transfer effectiveness and spreading ratio, it might not always be the case. For an order of magnitude understanding, when the diffusion timescale (τ) becomes less than the droplet interaction timescale (t_c) , increasing the spreading area may not have an impact on the total heat transfer. In such a case, the spreading fluid will exchange all/most of the available thermal energy even before the droplet spreads fully on the surface. The diffusion timescale depends on the thermophysical properties of the substrate and the fluid and can be estimated as follows:

$$\tau \sim \frac{L^2}{\alpha},$$
 (6)

where τ is the diffusion time, L is the diffusion length (here, it is assumed to be of the order of liquid film thickness when the droplet is fully expanded), and α is the thermal diffusivity of the liquid. Qualitatively, for the experiments performed in the current study, the diffusion timescale for the water film (from Equation 6) is of the order of 100 ms, which is significantly greater than the droplet interaction timescale \sim O(10) ms. Therefore, we observe a positive correlation between heat transfer effectiveness and the spreading ratio.

Next, we highlight the impact of contact time (t_c) on the overall heat exchange during droplet impact on a cold SHP surface. Contact

time defines the total duration for which the impacting drop is in contact with the SHP surface and is varied by changing the impact height among various experiments. Interestingly, our results show that, unlike the contact area, the heat transfer does not greatly depend on the contact time of the impacting droplet, on a given surface. Figure 6a plots the nondimensional heat exchange (Q') against the contact time (t_c) , which suggests a negligible dependency. Please note that changing height also affects the maximum spreading (as shown in Figure 4b), which is applicable in Figure 6a as well. Nonetheless, with an increase in contact time, the heat transfer effectiveness seems unaffected.

To understand the possible reasons, first, we illustrate and compare (see Figure 6b) the temporal evolution of the contact diameter for various impact heights and hence contact time. Interestingly, the spreading time (t_s) remains almost constant (the green-shaded region in Figure 6b) with h and the retraction time (t_r) reduces slightly (the yellow-shaded region in Figure 6b) with increasing h due to a faster droplet rebound (yellow-filled circle markers largest impacting height). The high-speed time-lapse images shown in Figure 7 highlight how the lower contact time for h = 7 cm manifests itself as reduced contact area (red lines in Figure 7b represent the instantaneous contact diameter) during the retraction stage. For instance, for the experiments shown in Figure 6b, the droplet impacting the surface with h = 7 cm leaves the surface at 10 ms (Figure 7b); however, the droplet impacting the surface with a lower height (h = 3 cm) still has ~ 1 mm contact diameter (red line in Figure 7b at 10 ms represents the contact diameter) with the surface (Figure 7b). A faster reduction in retraction stage contact area for higher impacting height can be expected to cancel out the effect of increased maximum spreading area (see Figure 7a at 3 ms), to some extent. However, as shown in Figure 3b, the retraction stage has lower heat transfer which results in an insignificant effect of reduced contact time on the heat transfer.

Having obtained the heat transfer dependency on contact time, we can realize that while the contact area has a positive power law, $Q' \sim (R_{\text{max}}/R)^{1.6}$, contact time has a negligible impact on heat transfer

FIGURE 7 Time-lapse optical images showing faster droplet retraction for higher impact height experiment. (a) High-speed snapshots of droplet spreading stage for h = 3 cm and h = 7 cm. Here, the droplet impacts with $T_1 = 298$ K on a superhydrophobic (SHP) surface at $T_5 = 278$ K. (b) High-speed snapshots of droplet retraction stage for h = 3 cm and h = 7 cm. The red line represents the instantaneous contact diameter during the retraction stage. Note that despite a larger spreading, the droplet impacting with greater height bounces back faster due to higher retraction velocity.

between an impacting droplet and the substrate. This helps in resolving the ambiguity on the role of contact time and contact area on the droplet impact heat transfer. Importantly, the spatially and temporally resolved 3D heat transfer solution reveals that the role of the contact area outweighs the effect of a decrease in contact time. This can be attributed to the effect of contact time in later stages of retraction which does not have a significant heat transfer. Therefore, simply decreasing the overall contact time may not have a big impact as the later stages of retraction contribute less to the overall heat transfer. For this, surfaces with shorter spreading times can prove to be more beneficial.

CONCLUSION

Impacting droplets are a common phenomenon in both industrial and biological systems such as spray cooling, fuel injection, spray coating, fire suppression, metal quenching, and rainwater shedding by animals for thermal management. While the applications seem diverse, the need to control and tune the droplet impact heat transfer ties them together. Inherently, the short-lived heat transfer during droplet impact depends on several factors such as fluid, substrate thermal properties, droplet size, spreading velocity, impacting velocity, and temperature difference between the droplet and substrate. Among these, how much the droplet spreads (contact area) and how long the droplet stays in contact (contact time) with the substrate have the

potential to significantly affect the heat transfer. We demonstrate the use of spatially and temporally resolved IR thermography to accurately capture the solid-liquid interface heat transfer during a droplet impact on a cold SHP surface. Our approach combines IR thermography with COMSOL simulations to quantify the individual roles of contact area and contact time on the heat transfer during droplet impact. The results highlight how the maximum spreading and actual contact area impact the heat transfer during droplet impact. Interestingly, the results show that contact area has a dominant effect on the heat transfer as compared to contact time. Moreover, contact time does not have any significant impact on the total heat transfer. We attribute this to the low heat transfer during the retraction stages of the droplet. Therefore, rather than altering the contact time, tuning the spreading time may prove to be more beneficial to tuning the heat transfer.

METHODS

Detailed experimental procedures and data analysis are provided in the Supporting Information.

ACKNOWLEDGMENTS

The experimental section of this work is supported by the National Science Foundation grant number 2047727. The conversion of IR-imaging to surface heat flux distribution simulation and analysis is supported

Droplet - WILEY - 9 of 9

by the Office of Naval Research grant number N00014-24-1-2086. All SEMs were performed in the UCSB Nanofabrication Facility, an open access laboratory.

CONFLICT OF INTEREST STATEMENT

The authors declare no conflicts of interest.

ORCID

Vijay Kumar https://orcid.org/0000-0002-6153-2313

Yangving Zhu https://orcid.org/0000-0001-9185-3161

REFERENCES

- 1. Han X, Li J, Tang X, et al. Droplet bouncing: fundamentals, regulations, and applications. *Small*. 2022;18:2200277.
- Shiri S, Bird JC. Heat exchange between a bouncing drop and a superhydrophobic substrate. Proc Natl Acad Sci USA. 2017;114:6930-6935.
- Mishchenko L, Hatton B, Bahadur V, Taylor JA, Krupenkin T, Aizenberg J. Design of ice-free nanostructured surfaces based on repulsion of impacting water droplets. ACS Nano. 2010;4:7699-7707.
- Wang L, Tian Z, Jiang G, et al. Spontaneous dewetting transitions of droplets during icing & melting cycle. Nat Commun. 2022;13:378.
- Gauthier A, Symon S, Clanet C, Quéré D. Water impacting on superhydrophobic macrotextures. Nat Commun. 2015;6:8001.
- Yun S. Bouncing of an ellipsoidal drop on a superhydrophobic surface. Sci Rep. 2017;7:17699.
- Nguyen TB, Park S, Lim H. Effects of morphology parameters on anti-icing performance in superhydrophobic surfaces. Appl Surf Sci. 2018;435:585-591.
- 8. Hoque MJ, Ma J, Rabbi KF, et al. Perspectives on superhydrophobic surface durability. *Appl Phys Lett.* 2023;123:110501.
- Lv J, Song Y, Jiang L, Wang J. Bio-inspired strategies for anti-icing. ACS Nano. 2014;8:3152-3169.
- Tao R, Liang G, Dou B, Wu J, Li B, Hao C. Oblique pancake bouncing. Cell Rep. Phys Sci. 2022;3:100721.
- Shu Y, Chu F, Hu Z, et al. Superhydrophobic strategy for natureinspired rotating microfliers: enhancing spreading, reducing contact time, and weakening impact force of raindrops. ACS Appl Mater Interfaces. 2022;14:57340-57349.
- 12. Bird JC, Dhiman R, Kwon HM, Varanasi KK. Reducing the contact time of a bouncing drop. *Nature*. 2013;503:385-388.
- Lathia R, Modak CD, Sen P. Two modes of contact-time reduction in the impact of particle-coated droplets on superhydrophobic surfaces. *Droplet*. 2023;2:e89.
- Yu Y, Cui W, Song L, et al. Design of organic-free superhydrophobic TiO2 with ultraviolet stability or ultraviolet-induced switchable wettability. ACS Appl Mater Interfaces. 2022;14:9864-9872.
- Ding B, Wang H, Zhu X, Chen R, Liao Q. Water droplet impact on superhydrophobic surfaces with various inclinations and supercooling degrees. Int J Heat Mass Transf. 2019;138:844-851.
- 16. Weisensee PB, Tian J, Miljkovic N, King WP. Water droplet impact on elastic superhydrophobic surfaces. *Sci Rep.* 2016;6:30328.
- 17. Wang H, Liu C, Zhan H, Liu Y. Droplet asymmetric bouncing on inclined superhydrophobic surfaces. *ACS Omega*. 2019;4:12238-12243.
- 18. Aboud DGK, Kietzig AM. On the oblique impact dynamics of drops on superhydrophobic surfaces. Part II: restitution coefficient and contact time. *Langmuir*. 2018;34:9889-9896.

- Hu Z, Chu F, Lin Y, Wu X. Contact time of droplet impact on inclined ridged superhydrophobic surfaces. *Langmuir*. 2022;38:1540-1549.
- Shu Y, Hu Z, Feng Y, Wu X, Dong Z, Chu F. Prince Rupert's drop bouncing on high-speed moving superhydrophobic surfaces. *Int Commun Heat Mass Transf*. 2023;148:107049.
- 21. Chen Y, Fu Y, Huang J, Luo Z, Mo D, Lyu S. Droplet bouncing on hierarchical branched nanotube arrays above and below the freezing temperature. *Appl Surf Sci.* 2016;375:127-135.
- Ko YS, Kim J, Ryu S, Han J, Nam Y, Lee C. Influence of early drop bouncing on heat transfer during drop impact. *Int Commun Heat Mass Transf*. 2022;137:106235.
- Gibbons MJ, Di Marco P, Robinson AJ. Local heat transfer to an evaporating superhydrophobic droplet. *Int J Heat Mass Transf*. 2018:121:641-652.
- Teodori E, Pontes P, Moita AS, Moreira ALN. Thermographic analysis of interfacial heat transfer mechanisms on droplet/wall interactions with high temporal and spatial resolution. Exp Therm Fluid Sci. 2018;96:284-294.
- Guo C, Maynes D, Crockett J, Zhao D. Heat transfer to bouncing droplets on superhydrophobic surfaces. Int J Heat Mass Transf. 2019;137:857-867.
- 26. Alizadeh A, Yamada M, Li R, et al. Dynamics of ice nucleation on water repellent surfaces. *Langmuir*. 2012;28:3180-3186.
- Lipson N, Chandra S. Cooling of porous metal surfaces by droplet impact. Int J Heat Mass Transf. 2020;152:119494.
- Schmidt JB, Roisman IV, Tropea C, Hussong J. Heat flux during a drop train impact in the drop rebound regime. Exp Therm Fluid Sci. 2023:145:110897.
- Bucci M, Richenderfer A, Su GY, McKrell T, Buongiorno J. A mechanistic IR calibration technique for boiling heat transfer investigations. *Int J Multiph Flow.* 2016;83:115-127.
- Li J, Weisensee PB. Low Weber number droplet impact on heated hydrophobic surfaces. Exp Therm Fluid Sci. 2021;130:110503.
- Gholijani A, Schlawitschek C, Gambaryan-Roisman T, Stephan P. Heat transfer during drop impingement onto a hot wall: the influence of wall superheat, impact velocity, and drop diameter. *Int J Heat Mass Transf*. 2020:153:119661.
- Guggilla G, Narayanaswamy R, Pattamatta A. An experimental investigation into the spread and heat transfer dynamics of a train of two concentric impinging droplets over a heated surface. Exp Therm Fluid Sci. 2020;110:109916.
- 33. Zupančič M, Gregorčič P, Bucci M, Wang C, Aguiar GM, Bucci M. The wall heat flux partitioning during the pool boiling of water on thin metallic foils. *Appl Therm Eng.* 2022;200:117638.

SUPPORTING INFORMATION

Additional supporting information can be found online in the Supporting Information section at the end of this article.

How to cite this article: Kumar V, Fu Q, Szeto H, Zhu Y. Heat transfer during droplet impact on a cold superhydrophobic surface via interfacial thermal mapping. *Droplet*. 2024;3:e124. https://doi.org/10.1002/dro2.124